

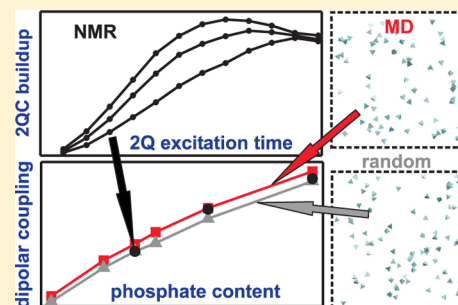
Assessing the Phosphate Distribution in Bioactive Phosphosilicate Glasses by ^{31}P Solid-State NMR and Molecular Dynamics Simulations

Baltzar Stevansson, Renny Mathew, and Mattias Edén*

Physical Chemistry Division, Department of Materials and Environmental Chemistry, Arrhenius Laboratory, Stockholm University, SE-106 91 Stockholm, Sweden

S Supporting Information

ABSTRACT: Melt-derived bioactive phosphosilicate glasses are widely utilized as bone-grafting materials for various surgical applications. However, the insight into their structural features over a medium-range scale up to ~ 1 nm remains limited. We present a comprehensive assessment of the spatial distribution of phosphate groups across the structures of 11 Na_2O – CaO – SiO_2 – P_2O_5 glasses that encompass both bioactive and nonbioactive compositions, with the P contents and silicate network connectivities varied independently. Both parameters are known to strongly influence the bioactivity of the glass in vitro. The phosphate distribution was investigated by double-quantum ^{31}P nuclear magnetic resonance (NMR) experiments under magic-angle spinning (MAS) conditions and by molecular dynamics (MD) simulations. The details of the phosphate-ion dispersion were probed by evaluating the MD-derived glass models against various scenarios of randomly distributed, as well as clustered, phosphate groups. From comparisons of the P–P interatomic-distance spreads and the statistics of small phosphate clusters assessed for variable cutoff radii, we conclude that the spatial arrangement of the P atoms in phosphosilicate glasses is well-approximated by a statistical distribution, particularly across a short-range scale of ≤ 450 pm. The primary distinction is reflected in slightly closer P–P interatomic contacts in the MD-derived structures over the distance span of 450–600 pm relative to that of randomly distributed phosphate groups. The nature of the phosphate-ion dispersion remains independent of the silicate network polymerization and nearly independent of the P content of the glass throughout our explored parameter space of 1–6 mol % P_2O_5 and silicate network connectivities up to 2.9.



1. INTRODUCTION

Several phosphosilicate glasses are termed “bioactive” because a strong bone–glass interface develops on their contact with body fluids.^{1–3} Some melt-derived *bioactive glass* (BG) compositions are exploited as bone grafting materials in maxillofacial, periodontal, and orthopedic surgery,^{1–3} notably the “45S5 Bioglass” with the stoichiometric formula $24.4\text{Na}_2\text{O}$ – 26.9CaO – 46.1SiO_2 – $2.6\text{P}_2\text{O}_5$.⁴ A relatively rapid glass degradation, followed by the formation of a biomimetic hydroxy-carbonate apatite (HCA) surface layer via an amorphous calcium phosphate (ACP) precursor phase are prerequisites for efficient bone-bonding properties, i.e., a high in vitro/vivo bioactivity.^{1,2}

Straightforward bioactivity predictions are hampered by the complex interplay between various structure/composition factors dictating the bioactivity of Na_2O – CaO – SiO_2 – P_2O_5 glasses and their analogues, coupled with an incomplete understanding of the structural modifications occurring over (sub)-nanometer scales when the glass composition alters. Most of the current structural insight of silicate-based BGs derives from solid-state nuclear magnetic resonance (NMR) spectroscopy,^{5–20} molecular dynamics (MD) simulations,^{12,20–25} and to a lesser extent, diffraction techniques.^{15–17}

A Na–Ca–Si–P–O glass comprises cross-linked rings and chains of interconnected SiO_4 groups. Introducing $\text{Na}^+/\text{Ca}^{2+}$

glass modifiers to a silica melt reduces the silicate network topology due to the breaking of Si–O–Si linkages, whereupon bridging oxygen (BO) atoms are converted into nonbridging oxygen (NBO) ions that charge balance the modifier cations.⁵ We adopt the “ Q_n^{Si} ” notation for a SiO_4 (and “ Q_n^{P} ” for a PO_4) tetrahedron that accommodates n BO atoms and $4 - n$ NBO ions.⁵ The *silicate network connectivity*, here denoted $\bar{N}_{\text{BO}}^{\text{Si}}$,²⁶ represents the *average* number of BO atoms per SiO_4 moiety.^{26–28} Relatively fragmented glass networks, built primarily from Q_2^{Si} groups, are believed to be of pivotal importance for the glass degradation in aqueous media,^{27,28} with the range $2.0 \lesssim \bar{N}_{\text{BO}}^{\text{Si}} \lesssim 2.6$ recently suggested as a prerequisite for high in vitro bioactivity.²⁶

It is well-established that P enters amorphous silicates predominantly as *orthophosphate* (Q_0^{P}) species, provided that the reservoir of modifier cations is sufficiently large to potentially charge-balance all PO_4^{3-} anions.^{5–8,26,29} This feature is important for ensuring readily leached PO_4^{3-} species that together with the concurrent Ca^{2+} ion release facilitate ACP/HCA formation in (simulated) body fluids.^{1–3} While all BG options in current clinical usage comprise a relatively low

Received: May 9, 2014

Revised: June 25, 2014

Published: June 26, 2014



Table 1. Glass Compositions^a

label	$a\text{Na}_2\text{O}$	$b\text{CaO}$	$c\text{SiO}_2$	$d\text{P}_2\text{O}_5$	$x_{\text{P}}^{\text{nom}} (x_{\text{P}}^{\text{exp}})$
BG _{2,6} (2.1) ^b	0.244(0.230) (0.229)	0.269(0.262) (0.255)	0.461(0.478) (0.486)	0.026(0.029) (0.030)	0.018(0.020) (0.021)
BG _{6,0} (2.1)	0.221(0.207)	0.324(0.315)	0.395(0.412)	0.060(0.065)	0.041(0.044)
BG _{1,0} (2.5)	0.192(0.181)	0.249(0.250)	0.549(0.559)	0.010(0.010)	0.007(0.007)
BG _{2,0} (2.5)	0.197(0.191)	0.257(0.258)	0.526(0.527)	0.020(0.024)	0.014(0.017)
BG _{4,0} (2.5) ^b	0.209(0.179) (0.193)	0.271(0.274) (0.254)	0.480(0.503) (0.509)	0.040(0.045) (0.044)	0.028(0.031) (0.030)
BG _{6,0} (2.5) ^b	0.219(0.204) (0.201)	0.287(0.285) (0.274)	0.434(0.446) (0.460)	0.060(0.064) (0.065)	0.041(0.043) (0.044)
BG _{2,6} (2.7)	0.202(0.194)	0.222(0.214)	0.550(0.560)	0.026(0.032)	0.018(0.022)
BG _{2,0} (2.9)	0.165(0.151)	0.215(0.206)	0.600(0.623)	0.020(0.020)	0.014(0.014)
BG _{3,0} (2.9)	0.172(0.161)	0.224(0.226)	0.574(0.583)	0.030(0.030)	0.021(0.021)
BG _{4,0} (2.9)	0.179(0.162)	0.233(0.226)	0.548(0.572)	0.040(0.040)	0.028(0.027)
BG _{6,0} (2.9)	0.193(0.172)	0.252(0.244)	0.495(0.524)	0.060(0.060)	0.040(0.040)

^aThe BG _{p} ($\bar{N}_{\text{BO}}^{\text{Si}}$) glasses are grouped according to increasing silicate network connectivity ($\bar{N}_{\text{BO}}^{\text{Si}}$) and P₂O₅ content (p mol % P₂O₅). The coefficients $\{a, b, c, d\}$ specify the nominally batched $a\text{Na}_2\text{O} - b\text{CaO} - c\text{SiO}_2 - d\text{P}_2\text{O}_5$ oxide equivalents with $a + b + c + d = 1$. Values within parentheses are compositions obtained via scanning electron microscopy and energy-dispersive X-ray spectroscopy; see Mathew et al.²⁰ $x_{\text{P}}^{\text{nom}}$ and $x_{\text{P}}^{\text{exp}}$ correspond to the nominal and EDS-analyzed atomic fraction of P, respectively. ^bThe second row lists the analyzed compositions of separately prepared glass samples incorporating 0.1 wt % of Fe₂O₃, as reported in refs 19 and 20; see the Supporting Information.

amount of P₂O₅ (<3 mol %),^{1–3} several studies suggest that the bioactivity correlates positively with the P content.^{2,30–33} On the basis of numerous literature data, we recently proposed that the in vitro bioactivity grows *monotonically* for increasing orthophosphate content.²⁶ Yet, three fundamental structural aspects of P, all having bearings on the bioactivity, are still debated:

- (1) *To what extent are high-connectivity $\text{Q}_p^{n>0}$ phosphate moieties present and how do their amounts depend on the glass composition?* Non-negligible Q_p^1 populations prevail in modifier-rich phosphosilicate glass structures,^{7–10,13,19,20} where MD simulations consistently reveal significant fractional populations (>15%) thereof.^{12,20–24} The initial NMR-based experimental reports on the $\{\text{Q}_p^n\}$ speciation of the archetypical “45SS” Bioglass^{1,4} concluded the sole presence of orthophosphate groups.^{12,15} However, more recent quantifications of the minor Q_p^1 populations revealed 4% and 8% for 45SS (ref 20) and its Na-free Ca–Si–P–O analogue,¹⁸ respectively, with the discrepancies between these estimates partly stemming from experimental uncertainties but primarily from an *expected* dependence of the precise $\{\text{Q}_p^0, \text{Q}_p^1\}$ populations on the relative Ca/Na content of the glass.⁹ Grussaute et al. provided evidence for the presence of significant Q_p^1 fractional populations (x_{P}^1) in modifier-rich Na–Ca–Si–P–O glasses with low P contents and relatively high $\bar{N}_{\text{BO}}^{\text{Si}}$ values, further demonstrating that x_{P}^1 remained independent on the amount of P in the glass.⁹ We recently extended these inferences over a wider range of silicate network connectivities and P contents, encompassing most of the parameter space relevant for bioactive compositions.²⁰ A direct linear $x_{\text{P}}^1/\bar{N}_{\text{BO}}^{\text{Si}}$ correlation was furthermore established, with the Q_p^1 population increasing concomitantly with $\bar{N}_{\text{BO}}^{\text{Si}}$, as verified both by magic-angle spinning (MAS) ³¹P NMR and by MD

simulations.²⁰ While both methods provided fully consistent qualitative trends, the MD models predict 2.5–3 times larger x_{P}^1 values compared with the corresponding experimental estimates.

- (2) *Is the oxygen bridge of a Q_p^1 group preferentially shared with a Si or P neighbor?* The short-range nature of the chemical shift interaction implies that the ³¹P NMR peak position associated with a given Q_p^n group depends primarily on its number of BO linkages (n);⁵ hence, once n is fixed, standard MAS NMR experimentation cannot readily discriminate signals of ³¹P–O–Si fragments from those of ³¹P–O–P in amorphous materials. The prevailing attribution of Q_p^1 groups to diphosphate anions based on ³¹P MAS NMR spectra is arbitrary. Notwithstanding, MD modeling suggest a clear preference for P–O–Si motifs,^{12,20–25} which was recently confirmed by dipolar/ J -coupling-based NMR experimentation both in the contexts of mesoporous bioactive glasses³⁴ and in the melt-prepared BGs¹⁸ from the CaO–SiO₂–P₂O₅ system.

Whereas (1) and (2) have been addressed experimentally to reasonable detail, no consensus has hitherto been reached for the following issue:

- (3) *How are the phosphate groups spatially distributed in BG structures?* This subject remains a dark zone, without any direct experimental data available until very recently,^{18,19} primarily stemming from the difficulties in addressing such problems in *homogeneous* amorphous phases by traditional diffraction or electron microscopy techniques. Consequently, statements made in the literature have remained either vague or speculative. The mere absence of BO atoms at orthophosphate (Q_p^0) moieties has been taken to imply a glass-in-glass separation into Si-rich and P-rich domains.^{2,14,33} To our knowledge, however, no direct evidence thereof exists in melt-prepared bioactive glasses, notwithstanding that (i) bioinactive glass compositions, rich in SiO₂ (≥ 55 mol %) and with

relatively high P_2O_5 contents (≥ 6 mol %), are prone to phase-separate and/or crystallize^{35,36} (such *long-range* features are readily revealed by electron microscopy³⁷), as mirrored in difficulties in preparing them by standard melt-quench procedures; (ii) an analogous nanoscale phase separation indeed occurs for polymer-templated $CaO-SiO_2-P_2O_5$ mesoporous bioactive glasses (MBGs),^{38,39} whose pore-walls comprise nanometer-sized ACP clusters dispersed across the main silica-rich $CaO-SiO_2$ component.^{19,34,40–42} Note that such amorphous calcium phosphate clusters are distinct from analogous but ordered domains previously observed by electron diffraction in related mesoporous silica-based materials⁴³ or in melt-prepared BGs incorporating large amounts of both Mg and P.¹¹ For a melt-derived Na-free 45S5 analog, Fayon et al. proposed that the P species exist predominantly as small clusters of 5–6 PO_4^{3-} groups dispersed in the silicate matrix.¹⁸ Noteworthy, this model highlights structural inhomogeneities up to 1–2 nm, as opposed to any larger-scale phase separation across tens of nm and beyond.

A simple statistical distribution of P species in melt-derived BG structures is also suggested, where the orthophosphate groups occupy interstitial positions around the silicate network.^{13,19} Such a structural picture is largely supported by MD simulations,^{22–24} with the main distinction that the glass models feature closer P–P contacts than those of a statistical phosphate distribution (as explored further herein), particularly for glasses rich in either P or Si, whose structures were reported to exhibit a non-negligible phosphate clustering.^{22,23} Yet, MD studies only exist for a few BG compositions, and previous assessments did not strictly target the spatial P atom distribution itself, merely its indirect probing via the relative preference for P–P interatomic contacts compared with those of P–Si.

The present paper aims at advancing both the qualitative and quantitative insight into the spatial dispersion of P in a series of 11 $Na_2O-CaO-SiO_2-P_2O_5$ glasses that encompass both bioactive and nonbioactive compositions. They were designed such that the P content (n_p) and the silicate network connectivity, both known to strongly influence the glass bioactivity, are varied independently.²⁰ The glasses are labeled $BG_p(\bar{N}_{BO}^{Si})$, with \bar{N}_{BO}^{Si} ranging from 2.1 to 2.9 and $1.0 \leq p \leq 6.0$ representing the P_2O_5 content in mol % (see Table 1); most of them exhibit a constant molar ratio $n_{Na}/n_{Ca} = 1.54$. With the dependence of the short-range structural features on the $\{n_p, \bar{N}_{BO}^{Si}\}$ parameters already reported,²⁰ we here proceed to examine their potential bearings on the phosphate distribution. From results of advanced solid-state ^{31}P MAS NMR techniques, we recently inferred that the (ortho)phosphate groups probed for some of these Na–Ca–Si–P–O glasses overall obey a statistical distribution.¹⁹ However, new experimental ^{31}P NMR data obtained under slightly different conditions prompted us to re-examine this conclusion. An excellent agreement is observed between the revised ^{31}P NMR data and those obtained from MD simulations; while these new results do not significantly alter the qualitative conclusions by Mathew et al.,¹⁹ the phosphate dispersion in a wide series of $Na_2O-CaO-SiO_2-P_2O_5$ glasses is now examined quantitatively for the first time, where we further clarify the similarities and distinctions

between the P distribution in these glasses relative to that of a simple statistical scenario.

2. SCENARIOS OF UNIFORM, RANDOM, AND CLUSTERED PHOSPHATE GROUPS

As commented by Johnson et al.,⁴⁴ the definitions of ion “clustering” vary in the literature, where the various degrees of $PO_4^{3-}-PO_4^{3-}$ association in glasses may range from a *complete aggregation* similar to the clusters encountered in crystalline orthophosphates, to a *uniform/even* distribution featuring equal P–P interatomic distances throughout. The latter scenario is depicted in Figure 1a. On the other hand, a *random/statistical*

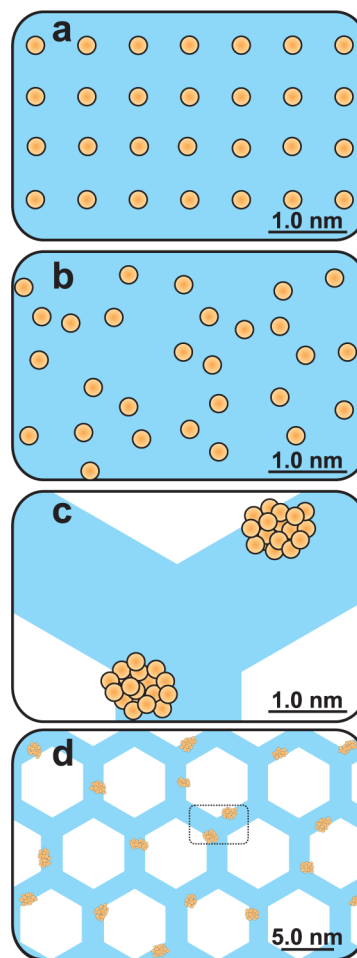


Figure 1. Schematic illustration of (a) uniform/even, (b) random, and (c) clustered distributions of phosphate groups (yellow circles) over a silicate glass (blue). (c and d) Pore-wall model of mesoporous bioactive glasses: while P resides in nanometer-sized clusters within each pore-wall (c), the clusters are homogeneously dispersed across the material (d), such that if probed over a large scale ≥ 10 nm, the real P atom distribution could be (incorrectly) conjectured as being either uniform or random.

phosphate ion distribution possesses an inherent degree of clustering, as illustrated in Figure 1b. Consequently, our assessments of clustering below generally aim at evaluating parameters such as P–P interatomic distances and the relative populations of phosphate aggregates in MD-derived glass models compared with the results from (independently generated) random or clustered distributions, as described in detail in Materials and Methods.

Note, however, that the outcome of comparisons between different structural models inevitably depends on the evaluation criteria. In the context of MBGs, panels c and d of Figure 1 illustrate the difficulties in assessing the arrangement of a minor species (here, P) spread across a dominating matrix (modified silica), as the conclusions depend on the length scale used to examine the distribution. Solid-state NMR, which may probe the structure across ~ 1 nm, revealed a pronounced orthophosphate clustering in the MBG pore walls (see Figure 1c).^{19,34} In contrast, a uniform/homogeneous P atom distribution was previously concluded^{38,39} from energy-dispersive X-ray spectroscopy (EDS) coupled with transmission electron microscopy that may only assess the *average* cation composition over tens of 10 nm. While the latter observation agrees well with the feature of *homogeneously distributed* orthophosphate *clusters* across the MBG pore-walls, as illustrated in Figure 1d, the phosphate-ion dispersion itself is clearly aggregated and only *appears* to be uniform when inspected over a larger length scale.

3. MATERIALS AND METHODS

3.1. Glass Sample Preparation and Characterization.

The BG_p($\bar{N}_{\text{BO}}^{\text{Si}}$) samples were prepared in batches of 6.0 g by a standard melt-quench procedure with precursors of Na₂CO₃ (99.9%), CaCO₃ (99.9%), and SiO₂ (99.99%) from ChemPur and NaH₂PO₄ (99.99%; Merck). After ball-milling for 12 h, each mixture was placed in a Pt crucible and heated for 4 h in an electric furnace at 950 °C to ensure complete CO₂ removal. The temperature was set to the final value in the range of 1350–1620 °C, with the highest temperatures required for compositions exhibiting a large P content and/or high $\bar{N}_{\text{BO}}^{\text{Si}}$ value. Each melt was held for 4 h prior to its quenching by immersing the bottom of the crucible in water. The evaporation losses during synthesis were typically $\lesssim 1.5$ wt %. Two sets of the BG_{2.6}(2.1), BG_{4.0}(2.5), and BG_{6.0}(2.5) compositions were prepared under identical conditions; one series included 0.1 wt % Fe₂O₃ and was utilized in our previous work,^{19,20} whereas all specimens used herein were devoid of paramagnetic doping. See the Supporting Information for further details.

Each glass specimen was examined by powder X-ray diffraction by using a PANalytical X'pert PRO MPD diffractometer and Cu K α_1 radiation. The data collection lasted for 4 h per sample, with 2θ ranging between 10°–70°. No crystalline phases were observed within an estimated lower detection limit of $\lesssim 1\%$. Scanning electron microscopy (SEM) with a JSM 7000F (JEOL) microscope in backscatter electron imaging mode (20 kV acceleration voltage) verified that each BG_p($\bar{N}_{\text{BO}}^{\text{Si}}$) sample constitutes a homogeneous glass phase, except for BG_{6.0}(2.9) that exhibits partial amorphous phase separation. Cation contents were estimated with a LINK INCA (Oxford instruments) EDS detector. Each reported composition resulted from averaging over ten analyses from distinct fragments, with the respective O content calculated to charge-balance the cations. The nominal and EDS-analyzed glass compositions overall agree well, as do the compositions of the “doped” and “undoped” BG_{2.6}(2.1), BG_{4.0}(2.5), and BG_{6.0}(2.5) samples (see Table 1), where the deviations remain within the uncertainty of the EDS measurements.

3.2. Solid-State NMR. All experimentation utilized a Bruker Avance-III spectrometer operating at the ³¹P Larmor frequency of -162.0 MHz at the external magnetic field of 9.4 T. Each sample in the form of a finely ground powder was packed in the central 1/3 portion of a 4 mm zirconia rotor to

minimize radio frequency (rf) inhomogeneity and spun at a MAS rate of 5.40 kHz (see the Supporting Information). The symmetry-based homonuclear dipolar recoupling sequence R20₂⁹ was used to generate ³¹P double-quantum coherences (2QC) from longitudinal polarization; we refer to Marin-Montesinos et al.⁴⁵ regarding its implementation in a double-quantum filtration (2QF) protocol and to Edén⁵ for a gentle introduction to such NMR experiments. A series of 2QF experiments with progressively lengthened 2QC excitation intervals (τ_{exc}) was performed to monitor the 2QC buildup, sampled at each completed R20₂⁹ period, i.e., at multiples of 370 μ s. At a given τ_{exc} -value, the 2QF efficiency was determined as the ratio between the integrated signal intensity after 2QF relative to that obtained from a “reference” NMR spectrum recorded directly by single pulses under otherwise identical experimental conditions. The 2QF data were corrected according to the procedure of Saalwächter et al.^{46–48}

All NMR experimentation involved a spectral window of 56 kHz, 40 s relaxation delays, and a total of 256–1680 accumulated signal transients per sample and τ_{exc} -value, with the largest numbers required for the shortest excitation intervals. ³¹P nutation frequencies of 54 kHz and 83 kHz were used for dipolar recoupling and the 90° read-out pulse, respectively. Further experimental information is given in the Supporting Information. NMR results targeting the short-range structures of the entire glass series were reported by Mathew et al.²⁰ The ³¹P NMR spectra recorded from the “undoped” BG samples used in the present work (not shown) are essentially indistinguishable from those of the doped samples that were presented in ref 20.

Polycrystalline calcium hydroxyapatite [HAP; Ca₅(PO₄)₃OH] was used as received from Aldrich (99.99% purity). Except for the sample confinement in the rotor, the HAP experimentation was identical to that described in the Supporting Information of Mathew et al.¹⁹

3.3. MD Simulations. Nearly all MD-stemming data presented herein resulted from the same glass models presented in Mathew et al.²⁰ that were generated for the *nominal* glass compositions listed in Table 1. Classical MD simulations were performed with the DLPOLY3 package^{49,50} for NVT ensembles of {Na, Ca, Si, P, O} atoms placed in a cubic box with periodic boundary conditions to match the experimental density. The simulation parameters are listed in Table S2 of the Supporting Information.

The computations involved a polarizable shell-model potential, where each cation carries its full formal charge, whereas the O²⁻ species are represented by core (O_C) and shell (O_S) units, coupled by a 300 THz harmonic oscillator and bearing charges of $z_{\text{C}} = +0.8482e$ and $z_{\text{S}} = -2.8482e$, respectively.^{22–24} A Buckingham potential parametrized all short-range O_S–O_S and cation–O_S pair interactions that were evaluated out to 0.8 nm. Coulombic interactions were calculated by a smoothed particle mesh Ewald summation⁵⁰ with a 1.2 nm real-space cutoff and an accuracy of 10^{–6}. The O–Si–O and O–P–O intratetrahedral angles were constrained with three-body truncated harmonic potentials.⁵⁰

Each melt-quench protocol started from a random atom configuration that was “equilibrated” for 100 ps at 3500 K, followed by a 10 K/ps cooling procedure down to 300 K in steps of 10 ps, and a subsequent equilibration for 200 ps, from which 7500 samples of the last 150 ps were averaged to yield the structural data. The equations of motion were integrated in steps of 0.2 fs using the velocity Verlet integrator, and the

temperature was controlled by a Berendsen thermostat with a time constant of 1.0 ps. This procedure was completed 2–4 times with different (random) initial atom configurations for each glass composition, from which the average value and uncertainty of each reported structural parameter were derived. In general, the data-spread across such independently generated glass models of a given $BG_p(\bar{N}_{BO}^{Si})$ composition was comparable to (and often larger than) those obtained for glasses exhibiting distinct \bar{N}_{BO}^{Si} values at a fixed P_2O_5 content. For the $BG_{2.6}(2.1)$, $BG_{4.0}(2.5)$, and $BG_{6.0}(2.5)$ glasses (i.e., those analyzed by ^{31}P NMR), we verified the absence of any significant variation of the effective ^{31}P – ^{31}P dipolar coupling constant (defined in Section 4.1) calculated from the MD-derived P atom coordinates when using slower cooling rates of 5 K/ps or 2 K/ps.

Although the Q_p^n speciations of the $BG_p(\bar{N}_{BO}^{Si})$ samples are dominated by orthophosphate groups, both ^{31}P NMR and MD simulations reveal the presence of significant Q_p^1 relative populations that amount to 4–20% and 17–55%, respectively, depending on the \bar{N}_{BO}^{Si} value; see Table S2 of the Supporting Information. All data reported herein is based on the entire phosphate speciation of each MD structure, except for very minor amounts of diphosphate groups (i.e., directly linked Q_p^1 – Q_p^1 pairs) that are only encountered in the P-richest BGs;²⁰ see Table S2 of the Supporting Information. As discussed in the Introduction, no experimental data support the existence of such moieties, but their significantly shorter ^{31}P –O– ^{31}P distances (≈ 300 pm) relative to the prevailing Q_p^0 – Q_p^0 and Q_p^0 – Q_p^1 contacts (> 350 pm) would, if included, lead to slightly increased effective coupling constants by up to 3%. Analogously, we utilized the total 2QF ^{31}P NMR signal intensity, which predominantly reflect through space Q_p^0 – Q_p^0 and Q_p^0 – Q_p^1 contacts, in the analysis.

3.4. Distribution Models. To assist the evaluation of the NMR/MD-derived structural data, two P atom distribution models—each involving ≈ 27000 P atoms, but without explicitly accounting for other elements—were generated within a cubic box, whose precise dimensions varied among the glass samples to match each respective P atom number density. The following models were considered:

- (i) A random dispersion of P atoms, “R(d_{min})”, subject to the constraint of a minimum P–P interatomic separation (d_{min}) within the range of 360–420 pm to ensure P–P contacts commensurate with orthophosphate-based structures. For instance, the shortest P–P interatomic distance among neighboring orthophosphate groups in the structures of β - $Ca_3(PO_4)_2$, α - $Ca_3(PO_4)_2$, $Ca_5(PO_3)_3OH$, and β - $NaCaPO_4$, amount to 380 pm,⁵¹ 411 pm,⁵² 411 pm,⁵³ and 422 pm,⁵⁴ respectively. Consequently, our selected d_{min} values may be taken as representative limits for the closest P–P contacts typically encountered in structures built from densely packed PO_4^{3-} anions. Moreover, $d_{min} = 360$ pm was selected, based on the (globally) shortest P–P interatomic distances ≈ 350 pm among orthophosphate groups in our MD glass models. The effective ^{31}P – ^{31}P dipolar coupling constant (see Section 4.1) representative for each R(d_{min}) model was obtained by a further averaging over 20 independently generated ensembles, each comprising ≈ 27000 P atoms. We stress that the present “R(d_{min})” model accounts implicitly for the presence of O atoms in the first coordination sphere of P and that

equivalent statistical cation-distribution models have been utilized in related contexts, such as for probing the dispersion of Na^+ ions in glasses.^{55–57}

- (ii) A random distribution of clusters, each comprising N phosphorus atoms; “CN”. Each cluster was obtained by selecting the P atom coordinates from one motif of N nearest-neighboring PO_4^{3-} groups within the structures of either α - $Ca_3(PO_4)_2$ [denoted CN(α Ca)], β - $Ca_3(PO_4)_2$ [CN(β Ca)], or β - $NaCaPO_4$ [CN(NaCa)]. Such clusters were randomly distributed with the constraint of a minimum inter-cluster distance of 460 pm to preclude their coalescence into larger aggregates. The reported effective ^{31}P – ^{31}P dipolar coupling constants representative of each such cluster scenario resulted from a further averaging over a large number (≈ 3400) of randomly selected (distinct) N -cluster motifs from each α/β - $Ca_3(PO_4)_2$ and β - $NaCaPO_4$ parent structure.¹⁹

4. RESULTS

4.1. Effective ^{31}P – ^{31}P Dipolar Coupling Constants from ^{31}P NMR. The net P–P interatomic contacts in a glass may be assessed by ^{31}P 2QF experiments utilizing dipolar recoupling under MAS conditions.^{5,19,46–48,58–61} Here, 2QC are excited in a series of experiments with incremented excitation intervals (τ_{exc}), as shown in Figure 2a. The 2QC buildup rate from a pair j – k of ^{31}P – ^{31}P nuclei in the structure increases concomitantly with the size of its through-space-mediated homonuclear dipolar coupling constant (b_{jk} in units of $rad\ s^{-1}$), which exhibits an inverse cubic relationship to the ^{31}P – ^{31}P internuclear distance r_{jk}

$$b_{jk} = -\frac{\mu_0}{4\pi} \hbar \gamma^2 r_{jk}^{-3} \quad (1)$$

where γ denotes the magnetogyric ratio of ^{31}P .

From eq 1 follows that a short distance is associated with a large coupling constant, whose 2QC buildup is more rapid than that of a ^{31}P – ^{31}P spin-pair featuring a large (small) value of r_{jk} (b_{jk}). However, the phosphate-ion distributions in structurally disordered materials, such as the present BGs, feature a large number of ^{31}P – ^{31}P pairs with distinct internuclear distances contributing to the net 2QF efficiency, which for short τ_{exc} values is well-approximated by the parabolic relationship^{19,47,48,58–60}

$$a_{2QF}(\tau_{exc}) \approx A(b_{eff}^{exp} \tau_{exc})^2 \quad (2)$$

where b_{eff}^{exp} is an experimentally determined effective ^{31}P – ^{31}P dipolar coupling constant^{47,48} and $A = 0.03646\ rad^{-2}$.¹⁹ The value of an experimental/calculated effective ^{31}P – ^{31}P dipolar coupling constant is related to those of the individual spin-pairs by^{47,62}

$$b_{eff}^2 = \sum_{j < k}^{all\ pairs} b_{jk}^2 \quad (3)$$

which according to eq 1 involves a sum over r_{jk}^{-6} . Consequently, the value of b_{eff} depends foremost on the j – k pair(s) exhibiting the shortest ^{31}P – ^{31}P internuclear separation(s). b_{eff}^2 relates to the pair distribution function [PDF; $g_{P-P}(r)$] according to⁵⁵

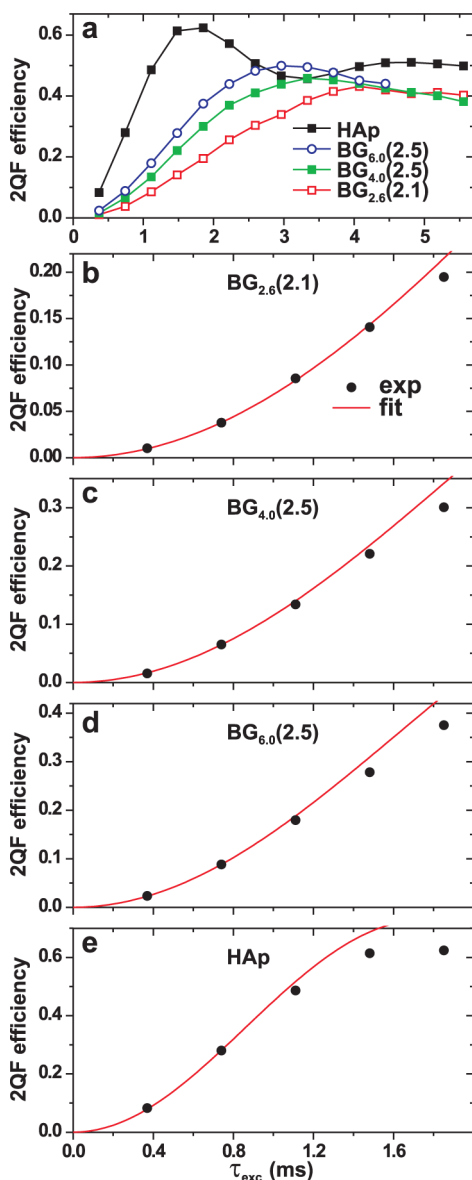


Figure 2. Experimental ^{31}P NMR double-quantum filtration (2QF) efficiencies plotted against the excitation interval for the as-indicated $\text{BG}_p(\bar{N}_{\text{BO}}^{\text{Si}})$ glass samples and polycrystalline calcium hydroxy-apatite (HAp). (b–e) Zooms of the initial 2QC buildup, shown together with curves of best-fit results based on the first two experimental data points. Experimental errors are within each symbol-size.

$$b_{\text{eff}}^2 = 4\pi\rho_p \int_0^\infty r^2 g_{p-p}(r) b^2(r) dr$$

$$= \frac{\mu_0^2}{4\pi} \hbar^2 \gamma^4 \rho_p \int_0^\infty r^{-4} g_{p-p}(r) dr \quad (4)$$

where $b(r)$ stems from eq 1 and ρ_p is the number density of P atoms in the glass.

Figure 2a plots 2QF efficiencies against τ_{exc} for a set of BG specimens, which feature increasing molar fractions $x(\text{P}_2\text{O}_5)$ in the range of 0.026–0.06, together with those from a reference sample of polycrystalline hydroxyapatite (HAp). The different NMR responses reflect distinct effective ^{31}P – ^{31}P dipolar coupling constants among the glasses, where a high (low) $b_{\text{eff}}^{\text{exp}}$ value provides a fast (slow) 2QC buildup rate, with the corresponding 2QF optimum occurring at a short (long)

excitation interval. Each coupling constant was extracted by fitting the initial 2QC buildup data to eq 2. While the numerical fitting accuracy improves by increasing the number of measurements (vide infra), the utilized set of $a_{2\text{QF}}(\tau_{\text{exc}})$ values must be restricted to a minimum because the approximation of eq 2 only captures the complicated 2QF dynamics faithfully in the limit $b_{\text{eff}}^{\text{exp}} \tau_{\text{exc}} \ll 1$, outside of which the $b_{\text{eff}}^{\text{exp}}$ value becomes systematically underestimated.^{19,48,60} We pursued our analysis by including either one, two, or three initial values of the $\{a_{2\text{QF}}(\tau_{\text{exc}})\}$ set from each glass, subject to the experimental sampling constraint $\Delta\tau_{\text{exc}} = 370 \mu\text{s}$. The corresponding best-fit results are presented in the Supporting Information, whereas Table 2 lists the selected options henceforth discussed, all derived from the first two 2QF amplitudes.

Panels b–d of Figure 2 display the initial 2QF NMR signal buildup and the associated curves obtained by fitting the first two $a_{2\text{QF}}(\tau_{\text{exc}})$ values to eq 2. Each upper vertical plot range is selected such that the experimental 2QF value at $\tau_{\text{exc}} = 1.9 \text{ ms}$ appears at a (nearly) fixed position in each graph to convey the similar qualities among the fits. These variable 2QF values reflect the distinct ^{31}P NMR-signal buildup rates among the glasses, whose associated effective dipolar coupling constants grow together with the P content of the sample (Table 2). Note the increased deviations between the experiments and best fits for $\tau_{\text{exc}} > 0.8 \text{ ms}$ when $b_{\text{eff}}^{\text{exp}}$ grows: for the case of $\text{BG}_{2.6}(2.1)$ in Figure 2b, the two-point fit obeys the experimental data excellently up to $\approx 1.5 \text{ ms}$ (4 points), whereas HAp in (e) reveals significant deviations.

The present $b_{\text{eff}}^{\text{exp}}$ values extracted from the $\text{BG}_{2.6}(2.1)$, $\text{BG}_{4.0}(2.5)$, and $\text{BG}_{6.0}(2.5)$ specimens are 15–20% higher than those previously reported by us for identical glass compositions.¹⁹ Two factors, discussed in detail in the Supporting Information, contribute to these revised results: (i) the omission of paramagnetic doping with 0.1 wt % Fe_2O_3 in the glass preparation, and (ii) the recording of NMR data by employing restricted sample volumes to improve the rf homogeneity. They provide roughly equal increases by 7–8% to the observed $b_{\text{eff}}^{\text{exp}}$ values, both being small but additive. The reliability of the new 2QF results from the BG samples may be appreciated from the data of the HAp specimen in Figure 2e. The best-fit effective dipolar coupling constants extracted by using either solely the first 2QF value, or the first two values, resulted in the respective estimates of $b_{\text{eff}}/2\pi = -661 \text{ Hz}$ and $b_{\text{eff}}/2\pi = -648 \text{ Hz}$, in excellent agreement with the value of -665 Hz calculated from the P atom coordinates of the HAp crystal structure.⁵³ In this case, the underestimation of our previous $b_{\text{eff}}^{\text{exp}}$ -value¹⁹ (by $\approx 8\%$) originated solely from the impact of rf inhomogeneity, which once reduced/eliminated, reproduced the theoretical coupling constant well within the experimental uncertainty of $\pm 8 \text{ Hz}$.

4.2. Effective ^{31}P – ^{31}P Internuclear Contacts: NMR versus MD Simulation Data. Figure 3 plots the experimentally determined ^{31}P – ^{31}P $b_{\text{eff}}^{\text{exp}}$ values together with the corresponding data calculated from the MD-generated structures, $b_{\text{eff}}^{\text{MD}}$, as well as that associated with phosphate-ion dispersion scenarios involving statistical distributions of either isolated orthophosphate groups or five-member clusters thereof (see Materials and Methods). The remarkably good agreement between the respective b_{eff} values derived from NMR and MD simulations in Figure 3a permits moving the spotlight onto unraveling the P atom distributions in the modeled structures, with increased confidence that they faithfully reflect those of the physical glasses. In the following, we seek a simplified

Table 2. P Distribution Data Obtained from ^{31}P NMR, MD Simulations, and Random Models^a

glass	$-b_{\text{eff}}/2\pi$ [Hz]			$\bar{r}_{\text{min}}/\text{pm}$		$\sigma_{\text{min}}/\text{pm}$		\bar{N}^{C}		x_1^{C}	
$\text{BG}_p(\bar{N}_{\text{BO}}^{\text{Si}})$	NMR	MD	R360–R420	MD	R360–R420	MD	R360–R420	MD	R360–R420	MD	R360–R420
$\text{BG}_{2.6}(2.1)$	221	228	222–178	534	559–584	112	131–116	1.23	1.33–1.11	0.82	0.76–0.90
$\text{BG}_{6.0}(2.1)$		350	340–276	462	466–501	56	78–62	1.95	2.13–1.34	0.52	0.51–0.76
$\text{BG}_{1.0}(2.5)$		147	138–110	675	719–736	205	211–197	1.09	1.11–1.04	0.92	0.90–0.96
$\text{BG}_{2.0}(2.5)$		210	192–154	565	600–623	146	153–138	1.23	1.23–1.08	0.82	0.82–0.92
$\text{BG}_{4.0}(2.5)$	291	291	277–223	485	506–536	76	102–86	1.54	1.58–1.20	0.63	0.65–0.84
$\text{BG}_{6.0}(2.5)$	342	355	339–276	464	467–500	58	78–63	1.96	2.13–1.35	0.57	0.51–0.75
$\text{BG}_{2.6}(2.7)$		238	219–175	540	563–589	121	134–118	1.31	1.32–1.11	0.78	0.77–0.90
$\text{BG}_{2.0}(2.9)$		202	197–156	572	594–618	139	151–135	1.22	1.25–1.09	0.82	0.81–0.92
$\text{BG}_{3.0}(2.9)$		253	235–188	523	544–571	113	123–108	1.30	1.38–1.13	0.73	0.73–0.88
$\text{BG}_{4.0}(2.9)$		295	273–220	485	509–538	76	103–88	1.51	1.57–1.20	0.65	0.66–0.84
$\text{BG}_{6.0}(2.9)$		357	334–270	466	469–504	66	80–65	1.96	2.05–1.32	0.54	0.52–0.77

^a $b_{\text{eff}}/2\pi$ represents the effective dipolar coupling constant, obtained either experimentally (NMR; uncertainty ± 8 Hz), from MD simulations (MD; uncertainty ± 13 Hz), or by random models (± 1 Hz), where “R360” and “R420” resulted by using $d_{\text{min}} = 360$ pm and $d_{\text{min}} = 420$ pm, respectively (see Materials and Methods). \bar{r}_{min} (± 5 pm) is the average value over all shortest P–P interatomic distances $\{\bar{r}_{\text{min}}\}$ in the structure, whereas σ_{min} (± 5 pm) is its associated distribution width. \bar{N}^{C} and x_1^{C} denote the average cluster size and fractional population of isolated phosphate groups, respectively, as obtained for a cutoff radius of $R^{\text{C}} = 450$ pm (see Section 4.4). Note that the small differences among the data of the random models from $\text{BG}_p(\bar{N}_{\text{BO}}^{\text{Si}})$ specimens with fixed p stem solely from their minor density variations.

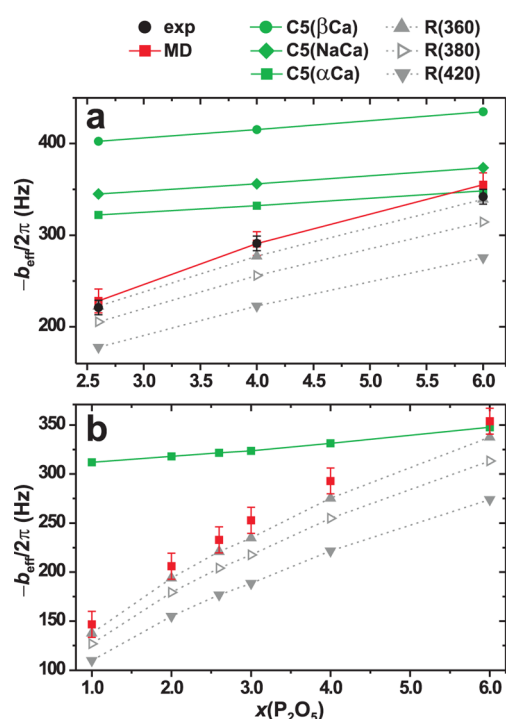


Figure 3. (a) Effective ^{31}P – ^{31}P dipolar coupling constants ($-b_{\text{eff}}/2\pi$) estimated from the $\text{BG}_{2.6}(2.1)$, $\text{BG}_{4.0}(2.5)$, and $\text{BG}_{6.0}(2.5)$ glasses, and plotted against the molar fraction of P_2O_5 in the glass. The b_{eff} values were determined either by ^{31}P NMR, or calculated from MD simulations and various models involving either randomly distributed P atoms [$R(d_{\text{min}})$; $d_{\text{min}} = \{360, 380, 420\}$ pm] or randomly distributed clusters of five phosphate groups selected from each structure of $\alpha\text{-Ca}_3(\text{PO}_4)_2$, $\beta\text{-Ca}_3(\text{PO}_4)_2$, and $\beta\text{-NaCaPO}_4$, denoted C5(αCa), C5(βCa), and C5(NaCa), respectively. (b) Plot of the effective coupling constants over the entire range of available P_2O_5 contents $1.0 \leq p \leq 6.0$ mol %, where b_{eff} is averaged over all glasses $\text{BG}_p(\bar{N}_{\text{BO}}^{\text{Si}})$ associated with constant p but variable $\bar{N}_{\text{BO}}^{\text{Si}}$ values (see Table 2).

model capturing the essentials of the “real” but complex phosphate-ion distribution and to further characterize the deviations from the latter. Our analysis centers around comparisons of the MD-derived P atom coordinates with their statistically distributed counterparts. Figure 4 depicts these respective models for the two glasses $\text{BG}_{2.0}(2.5)$ and $\text{BG}_{6.0}(2.5)$ that feature a low and high P_2O_5 content, respectively. Note that on a visual basis, they are virtually impossible to assign to “MD” or “random” models without a priori knowledge of their origins.

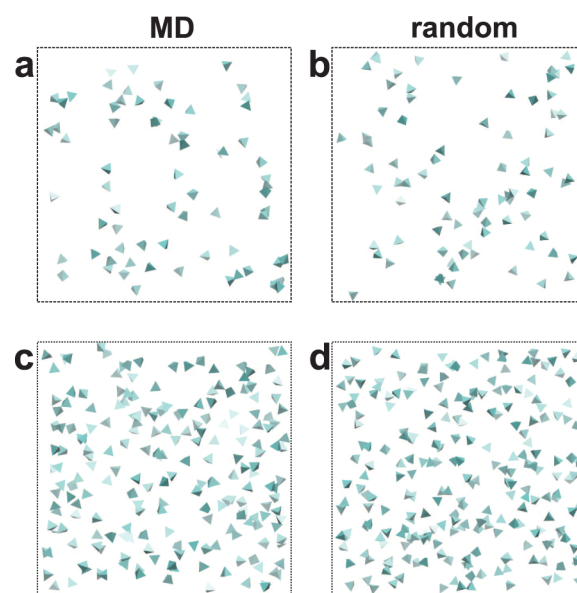


Figure 4. Graphical depiction of the P atom coordinates (center of tetrahedra) obtained from MD simulations (left panel) and a statistical R(380) distribution model (right panel) for the (a and b) $\text{BG}_{2.0}(2.5)$ and (c and d) $\text{BG}_{6.0}(2.5)$ glasses. The tetrahedra are only shown for visual purposes and have themselves no physical significance because the O atoms are only accounted for implicitly in the random model.

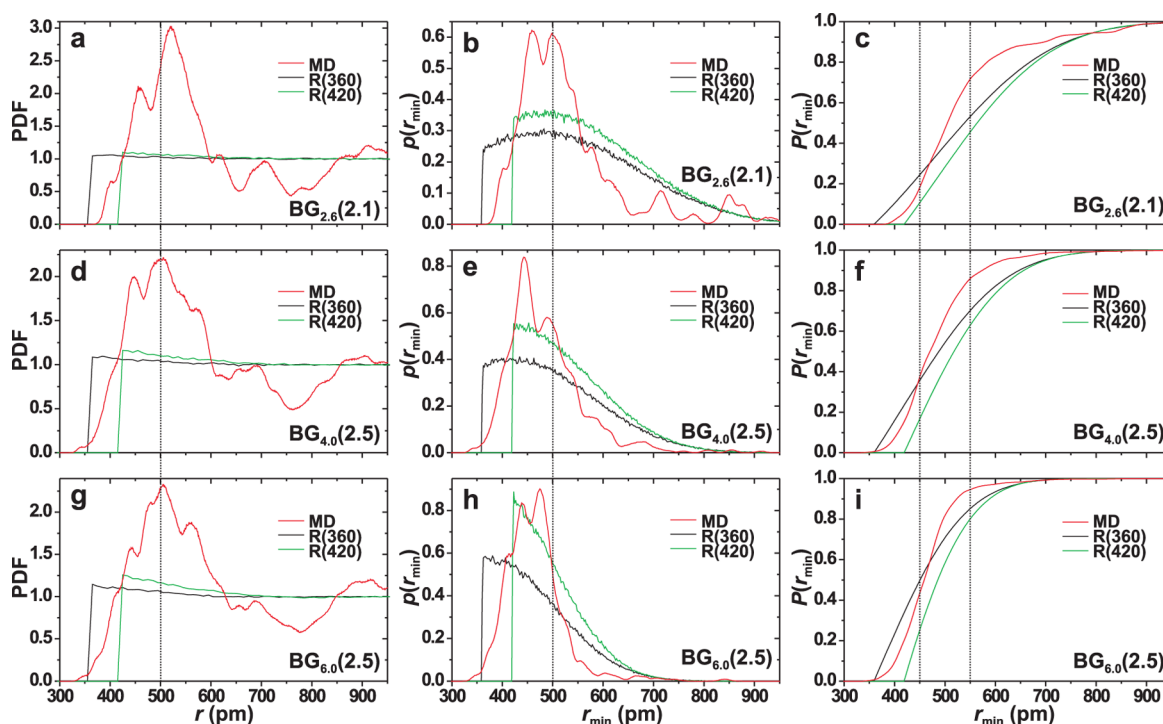


Figure 5. Comparisons of P–P interatomic distance-related data from MD simulations and random [R(360); R(420)] distribution models for three BG compositions featuring increasing P_2O_5 contents of 2.6 mol % (top panel), 4.0 mol % (middle), and 6.0 mol % (bottom). The left, middle, and right panels display pair distribution functions (PDFs), probability $p(r_{\min})$ of shortest P–P interatomic distances r_{\min} , and the corresponding cumulative probabilities $P(r_{\min})$, respectively.

The MD-derived effective dipolar couplings ($b_{\text{eff}}^{\text{MD}}$) are listed in Table 2. They grow markedly for increasing P content of the glass, whereas if $x(\text{P}_2\text{O}_5)$ remains fixed, the set of $b_{\text{eff}}^{\text{MD}}$ values reveals no significant variations on $\bar{N}_{\text{BO}}^{\text{Si}}$. Furthermore, the presence of the $\bar{N}_{\text{BO}}^{\text{Si}}$ -dependent Q_{P}^1 populations (listed in Table S2 of the Supporting Information) do not appear to affect the evaluation of P atom-distribution-associated observables/parameters, as confirmed by the data in Table 2. This is fortunate, given the overestimation of the x_{P}^1 fractions in the MD models,²⁰ but suggests that despite the distinctly different structural roles of the silicate network-associated Q_{P}^1 species, the nature of their spatial distribution is very similar to that of their orthophosphate (Q_{P}^0) counterparts. Consequently, Figure 3b presents b_{eff} values averaged over all $\text{BG}_p(\bar{N}_{\text{BO}}^{\text{Si}})$ structures sharing the same P_2O_5 content (p) but exhibiting distinct $\bar{N}_{\text{BO}}^{\text{Si}}$ values; for instance, the data from the $\text{BG}_{6.0}(2.1)$, $\text{BG}_{6.0}(2.5)$, and $\text{BG}_{6.0}(2.9)$ structures together form the effective coupling constant representative for $x(\text{P}_2\text{O}_5) = 0.06$.

An MD/NMR-derived effective ^{31}P – ^{31}P dipolar coupling constant conveys the aggregate P–P interatomic contacts in the structure, but it reveals no details about the underlying phosphate ion distribution. However, the latter may be assessed from the accordance between the experimental/modeled ($b_{\text{eff}}^{\text{exp}}$; $b_{\text{eff}}^{\text{MD}}$) values and those calculated ($b_{\text{eff}}^{\text{calc}}$) by assuming various P atom distribution scenarios. According to Figure 3b, the NMR/MD-derived effective P–P interatomic contacts are overall well-mimicked by a random distribution associated with $d_{\min} \approx 360$ pm, notably so with the experimental data (see Table 2). The deviations are explored further below. Yet, considering solely the effective dipolar interaction, the P-richest $\text{BG}_{6.0}(2.5)$ glass is potentially also commensurate with randomly distributed small clusters, such as those of five PO_4^{3-} groups extracted from the

$\alpha\text{-Ca}_3(\text{PO}_4)_2$ structure (Figure 3); however, as discussed below, such a scenario is precluded by other constraints.

4.3. P–P Interatomic Distance Distributions. Given that the most prominent contributions to $b_{\text{eff}}^{\text{exp}}$ (eq 3) stem from the ^{31}P – ^{31}P spin-pairs that exhibit the shortest internuclear distances in the structure (eq 1), it is instructive to compare those data from each MD-derived BG model with the respective distances obtained from uniformly and randomly distributed P species, the latter constrained by variable d_{\min} thresholds (see Materials and Methods). For each glass model obtained either from MD simulations or by a statistical $R(d_{\min})$ distribution, the set $\{r_{\min}^j\}$ was extracted by scanning over all P sites in the structure, with r_{\min}^j constituting the distance of site j to its nearest neighbor. The mean value (\bar{r}_{\min}) and distribution width (σ_{\min}) of each $\{r_{\min}^j\}$ set were calculated; they are compiled in Table 2.

For a uniform (even) phosphate-ion distribution, $\sigma_{\min}^{\text{uni}} = 0$, because all P–P interatomic separations are equal and considerably longer than those of any other dispersion model. For example, glasses incorporating 2.0 mol % and 6.0 mol % of P_2O_5 with uniformly distributed phosphate groups reveal P–P interatomic distances ≈ 980 pm and ≈ 690 pm, respectively, being 1.5–1.7 times longer than the corresponding shortest (average) distances $\bar{r}_{\min}^{\text{MD}}$ of ≈ 570 pm and ≈ 465 pm encountered in the MD-derived structures (Table 2). However, given that most of the space in the bulk glass is occupied by the silicate network and its associated $\text{Na}^+/\text{Ca}^{2+}$ cations for NBO ion charge-balancing, a simple uniform distribution scenario of the minor phosphate component is not anticipated to provide a reasonable description of BG structures. In contrast, Table 2 reveals only slightly longer P–P interatomic distances of $\bar{r}_{\min}^{\text{R}} \approx 600$ pm for the R(360) distribution from glasses incorporating 2.0 mol % P_2O_5 when compared with the MD-derived values.

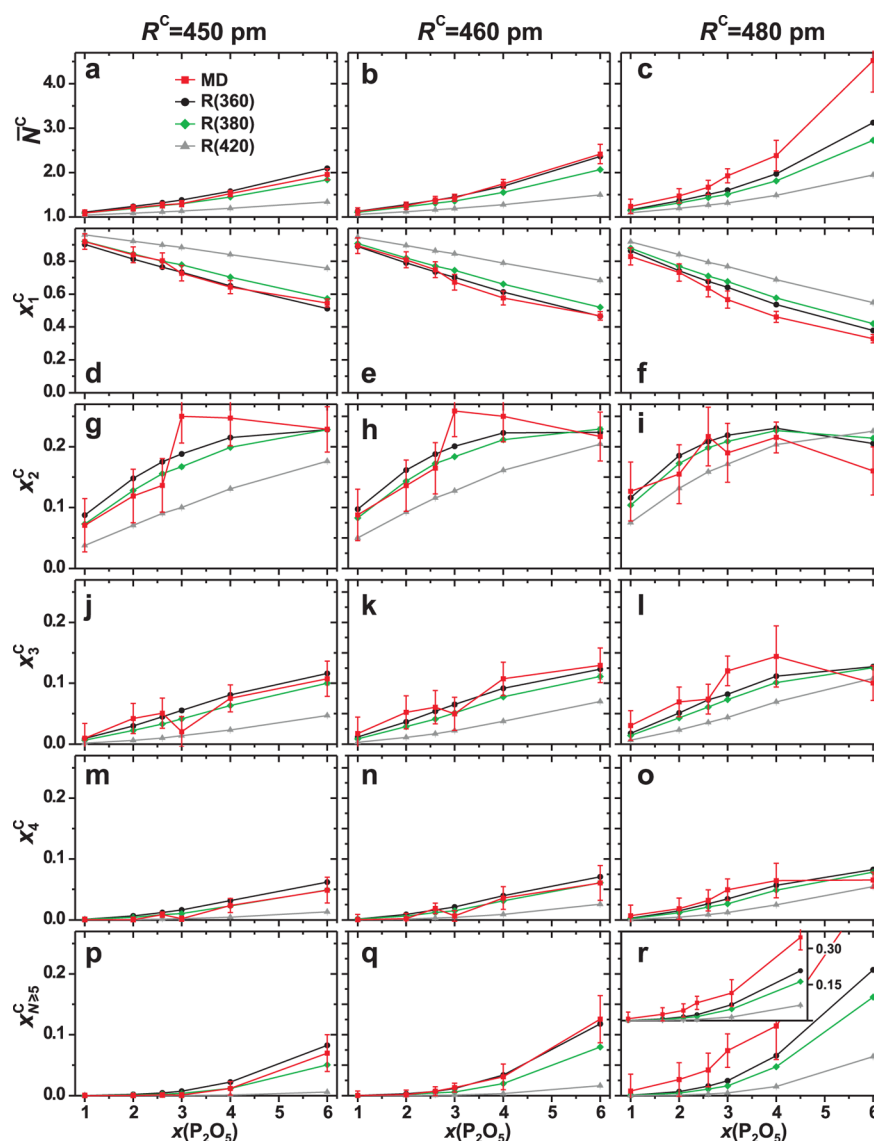


Figure 6. (a–c) Average phosphate-cluster size (\bar{N}^C) and (d–r) fractional populations (x_N^C) of N -clusters plotted against the P_2O_5 content of the glass, as obtained by requiring a minimum distance between nearest-neighboring P atoms of $R^C = 450$ pm (left panel), $R^C = 460$ pm (middle panel) and $R^C = 480$ pm (right panel). The data represent averages over the contributions from all glasses with a constant P content; they were obtained from MD simulations or random distributions of phosphate groups, as identified by the legend in (a). Note the much wider vertical scale employed in (d–f) relative to (g–r), and also that the graphs in (p–r) display net populations from all cluster sizes $N^C \geq 5$. The data uncertainties of the $R(d_{\min})$ models are within the symbol size.

The differences between the MD glass models and those representing statistically distributed P species generally shrink for increasing P_2O_5 content of the glass, such that nearly equal shortest P–P interatomic distances are observed for the P-richest structures exhibiting 6.0 mol % P_2O_5 : $\bar{r}_{\min}^{\text{MD}} \approx \bar{r}_{\min}^{\text{R}}$.

We next consider the *entire* set of P–P interatomic distances within each MD or statistical [R(360) and R(420)] distribution model. The left and middle columns of Figure 5 display their relevant P–P pair distribution functions [$g_{\text{P-P}}(r)$] and entire sets of shortest distances $\{r_{\min}^i\}$, respectively, for the $BG_{2.6}(2.1)$, $BG_{4.0}(2.5)$, and $BG_{6.0}(2.5)$ structures previously analyzed by ^{31}P NMR (see Figure 3a). Not surprisingly, the MD-associated PDFs differ significantly from the step-functional form of the random distributions. The former curves suggest some ordering of the phosphate ions, with peaks appearing from pairs whose P atoms are separated by around 400 pm, 450 pm, and 520 pm. For increasing P content of the glass, the number of such local

maxima grows, while each becomes more diffuse. As expected, the distribution $p(r_{\min})$ of *shortest* distances shifts toward closer P–P interatomic contacts for increasing phosphate content, while its accompanying distribution width (σ_{\min}) narrows (Figure 5). These trends are common for all MD/ $R(d_{\min})$ structural models, which primarily differ in their distribution widths, where the MD-generated σ_{\min} value is generally lower than those of the two statistical distributions [R(360) and R(420)] at a fixed P content of the glass (see Table 2).

The cumulative probability functions plotted in the right column of Figure 5 reveal that whereas the $P(r_{\min})$ function associated with R(360) rises quicker than its MD-derived counterpart across the range of shortest P–P interatomic distances $r_{\min} \lesssim 450$ pm (with the precise upper limit depending on the P content of the glass), the MD-generated probability function accumulates significantly faster for a larger distance span of 450–600 pm. The closer-than-random phosphate-ion

contacts across this range constitutes the primary distinction between the simulated glass structures and a simple statistical distribution; they account mainly for the slightly lower $b_{\text{eff}}^{\text{MD}}/b_{\text{eff}}^{\text{exp}}$ values obtained from the R(360) model relative to its $b_{\text{eff}}^{\text{MD}}/b_{\text{eff}}^{\text{exp}}$ counterparts in Figure 3. In the BG_{2.6}(2.1), BG_{4.0}(2.5), and BG_{6.0}(2.5) MD models, 18%, 37%, and 43% out of all *closest* P–P interatomic distances, respectively, occur within 450 pm. Very similar results apply for the R(360) model. However, if instead considering the corresponding fractions of distances $r_{\text{min}} \leq 550$ pm in the MD/R(360) structures, they display larger deviations according to 72/53%, 86/70%, and 95/85% for each respective glass. As for the aggregate $\{\bar{r}_{\text{min}}, \sigma_{\text{min}}\}$ distribution parameters, these discrepancies shrink for increasing P content of the glass, revealing a higher aggregation *tendency* of the P atoms in glasses featuring the lowest phosphate content. Consequently, when the amount of P grows, the set of shortest P–P interatomic distances in each MD glass model tends toward that of statistically distributed phosphate groups.

4.4. Cluster Statistics. To gain insight into the topological arrangement of the phosphate species in each glass structure, a “cluster statistics” was performed to locate and quantify aggregates of N^{C} phosphate groups, requiring P–P interatomic distances within a given threshold R^{C} between nearest neighbors of P atoms within the cluster. Each cluster size N^{C} is defined such that the distance from any P atom *inside* the cluster exceed R^{C} to its nearest P atom *outside* of the cluster. A phosphate moiety associated with a distance exceeding R^{C} to its nearest neighbor is referred to as “isolated”, i.e., $N^{\text{C}} = 1$. The cluster statistics were assessed for structures generated either by MD simulations or randomly distributed P species with d_{min} of 360 pm [R(360)], 380 pm [R380], and 420 pm [R(420)].

Initially, the threshold $R^{\text{C}} = 450$ pm was selected to explore if local structural motifs typical of crystalline Na/Ca-based orthophosphate phases may be present in the BGs. Table 2 compiles the average cluster size (\bar{N}^{C}) and fractional population of the isolated phosphate groups (x_1^{C}) obtained for each MD-derived glass model. The absence of any significant cluster formation is evidenced by average cluster sizes $1 \lesssim \bar{N}^{\text{C}} \lesssim 2$ encountered throughout the series of glasses, with $\bar{N}^{\text{C}} \approx 2$ only observed in the P-richest BGs incorporating 6 mol % P₂O₅, whereas the fraction of isolated phosphate groups out of the total P population consistently exceeds 50% in any BG structure for the as-assumed cutoff distance of 450 pm.

Given that all structures featuring a fixed P content exhibit very similar average cluster sizes and fractional populations of N^{C} clusters ($x_N^{\text{C}}; \sum_N x_N^{\text{C}} = 1$), those parameters were averaged to obtain one set $\{\bar{N}^{\text{C}}, x_N^{\text{C}}\}$ representative for each unique P₂O₅ content encountered within the glass series. The average cluster size, evaluated for increasing R^{C} -values, are plotted against $x(\text{P}_2\text{O}_5)$ in Figure 6 (panels a–c) for the MD and R(d_{min}) models. As expected, the results of the R(d_{min}) distribution depend strongly on the parameter d_{min} , with the \bar{N}^{C} values progressively growing as d_{min} decreases. However, at a fixed P content, the average cluster sizes associated with the R(360) model remain overall closest to those of the MD-derived counterparts, except for P-richest glasses with $x(\text{P}_2\text{O}_5) \geq 0.04$ and $R^{\text{C}} = 480$ pm, where larger \bar{N}^{C} values are observed in the MD-generated structures relative to randomly distributed P moieties. These trends are also mirrored by the fractional populations of isolated phosphate groups displayed in panels d–f of Figure 6.

Panels g–r of Figure 6 depict the populations of pairs, triplets, and larger phosphate aggregates. Within the scatter of

the MD data, the nature of its phosphate aggregation is overall well-mimicked by a statistical distribution subject to a minimum P–P interatomic distance $d_{\text{min}} \approx 360$ pm. When evaluated for short distance-cutoffs $R^{\text{C}} \leq 450$ pm (i.e., when requiring interatomic separations typical for crystalline orthophosphates), the R(360) model even reveals slightly higher populations of the largest phosphate aggregates relative to the MD-derived structure, whereas this picture reverses for larger thresholds $R^{\text{C}} \gtrsim 480$ pm, where the N^{C} distribution shifts toward larger cluster sizes in the MD model compared to its R(360) counterpart. These discrepancies reflect the overall closer P–P interatomic separations in the range of 450–600 pm observed from the MD-generated glasses compared to statistically distributed P atoms, as highlighted in Section 4.3 (see Figure 5).

Figure 7 depicts structural fragments observed from BGs incorporating low [BG_{2.6}(2.1); (a, b)] and high [BG_{6.0}(2.5);

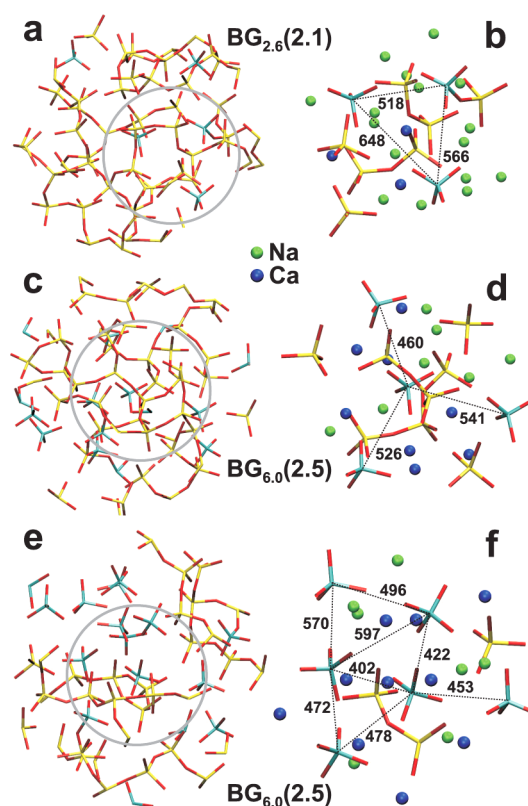


Figure 7. Structural motifs extracted from the (a and b) BG_{2.6}(2.1) and (c–f) BG_{6.0}(2.5) MD models, displayed over a radius of 2.0 nm (left panel). The right panel shows zooms over a radius of 1.2 nm [as marked by each circle in (a, c, and e)], where the Na⁺/Ca²⁺ cations are also displayed. Red, yellow, and cyan color depicts O, Si, and P atoms, respectively. The sets of shortest P–P interatomic distances (in picometers) are indicated in (b, d, and f). The fragments in (c and d) and (e and f) from the BG_{6.0}(2.5) structure represent “typical” and “clustered” phosphate constellations, respectively. Note that all P–P atom-pairs appearing outside the encircled area in (e) feature longer distances than the clustered motifs depicted in (f).

(c–f)] amounts of P₂O₅, respectively. The fragments in the left panel are shown over a larger radius of 2.0 nm that is further zoomed over a smaller radius of 1.2 nm in the right panel, with all shortest P–P interatomic distances marked in the latter. As expected, the motifs displayed for the BG_{6.0}(2.5) model reveals overall closer P–P interatomic contacts in the P-richest

structure relative to those associated with the lower P_2O_5 content of $BG_{2.6}(2.1)$ [i.e., “45SS”]. Figure 7f displays another structural fragment from $BG_{6.0}(2.5)$, illustrating how the most pronounced cluster formation may manifest in the P-richest BG samples. As opposed to the previous scenarios where the phosphate groups naturally distribute around the silicate-based network, which predominantly dictate the positions of the remaining species building the structure (Figure 7, panels a–d), the motif in (f) reveals essentially only phosphate groups surrounded by Na^+/Ca^{2+} cations that together occupy a larger space devoid of SiO_4 moieties.^{22,23} We stress, however, that whereas such phosphate constellations are encountered in the P-richest BG structures, they are *not* representative for their overall P atom dispersion and substantially increased amounts of P aggregates ($N^C \geq 5$) only manifest for large cutoffs $R^C \gtrsim 480$ pm (see the right panel of Figure 6).

5. DISCUSSION

5.1. Absence of Clusters Typical of Crystalline Phosphates. Figure 3 suggests that both the experimental and modeled effective ^{31}P – ^{31}P dipolar coupling constant of the $BG_{6.0}(2.5)$ specimen could be consistent with a structure featuring randomly distributed $N^C = 5$ clusters extracted from the α - $Ca_3(PO_4)_2$ structure. However, the cluster analysis of the previous section rules out such an option, as examined further below.

Both Table 2 and Figure 6 evidence that a non-negligible formation of aggregates larger than triplets and quartets of phosphate groups only manifests in the P-richest BGs. For instance, for the MD/R(360) models of the $BG_{6.0}(2.5)$ structure, about 5/9% and 30/21% of the total phosphate population reside in such $N^C \geq 5$ aggregates, when minimum distances of $R^C = 450$ pm and $R^C = 480$ pm are selected for the cluster statistics, respectively. For the $BG_{2.6}(2.1)$ glass, on the other hand, the corresponding numbers remain less than 4/2% even for the larger $R^C = 480$ pm cutoff radii. The similar total populations of such larger phosphate aggregates observed from the MD and R(360) models underscore that a statistical distribution readily accounts for the cluster formation of the MD-generated glass models for $R^C = 450$ pm; this cutoff is suitable for detecting phosphate aggregates typical of crystalline phases, such as HAp, β - $Ca_3(PO_4)_2$, and β -NaCaPO₄.^{51,53,54} Indeed, since most/all of their P–P interatomic distances between nearest-neighboring PO_4^{3-} groups are shorter than 450 pm, application of our cluster analysis results in one large aggregate, whereas the (unusually) loose phosphate-ion packing in the α - $Ca_3(PO_4)_2$ structure⁵² (mirrored in lower b_{eff} values for its phosphate-aggregates; see Figure 3 and Figure S1 of the Supporting Information) reveals that $\approx 30\%$ of the P reservoir is present as isolated PO_4^{3-} groups or pairs thereof, with the remaining constituting an infinitely large cluster.

From multiple-quantum coherence (MQC) based ^{31}P NMR experiments, Fayon et al.¹⁸ proposed that a Ca–Si–P–O glass structure featuring an identical P content and silicate network connectivity as $BG_{2.6}(2.1)$ (e.g., “45SS”) comprise $N^C = 5$ clusters that mimic fragments encountered in α - $Ca_3(PO_4)_2$. Nevertheless, as concluded by Mathew et al.¹⁹ and further corroborated by our present experimental and modeled data (e.g., Figures 3 and 6), a significant phosphate clustering is absent in BG structures of such low P content (2.6 mol % P_2O_5), at least for Na–Ca–Si–P–O glasses. Moreover, while P-rich BGs exhibit minor populations of phosphate aggregates exhibiting similar P–P interatomic separations as those

typically found in crystalline PO_4^{3-} -based phases, most of this “apparent clustering” is readily reconciled with the progressively shortened P–P interatomic distances naturally arising when additional phosphate groups enter the structure (nearly) statistically.

In conclusion, none of the structures exhibit any significant P atom aggregation consistent with structural motifs from crystalline phosphates, as suggested for a Ca–Si–P–O glass.¹⁸ However, these apparent discrepancies may also originate from the distinct glass systems studied: owing to a reported stronger Ca– PO_4 affinity relative to Na– PO_4 ,^{22–24} phosphate clustering effects may become emphasized in Ca–Si–P–O glasses relative to their Na-bearing analogs investigated herein and in ref 19. This is an interesting line for future investigations.

5.2. Nature and Composition-Dependence of the Phosphate Distribution. Table 2 reveals that the primary distinctions between the \bar{r}_{min} values of the modeled structures and statistically dispersed phosphate groups [$R(d_{min})$ with $d_{min} \approx 360$ pm] generally result for BGs associated with low P_2O_5 contents ≤ 2 mol %, whereas the differences between the two phosphate distributions shrink for increasing amount of P_2O_5 . This feature along with the cumulative probabilities $P(r_{min})$ plotted in Figure 5 suggest a slightly higher P clustering tendency in the BGs of lowest P_2O_5 contents, analogously with a previous report on the Na^+ cation dispersion in amorphous silicates⁵⁷ or the rare-earth-ion clustering versus rare-earth content in such glasses.⁴⁴ Moreover, the nature of the P atom distribution is essentially independent of the silicate network connectivity, as evidenced by several parameters of Table 2, such as (i) the effective dipolar coupling constants; (ii) the parameters $\{\bar{r}_{min}, \sigma_{min}\}$ associated with the shortest P–P interatomic separation observed for each phosphate group in the structure, as well as (iii) the average cluster size \bar{N}^C and its underlying populations $\{x_N^C\}$ of N^C clusters.

The invariance of the P atom dispersion on the silicate network connectivity (see Table 2) firmly establishes our previous conclusions drawn by 2QF ^{31}P NMR experiments from solely two glasses [$BG_{4.0}(2.5)$ and $BG_{4.0}(2.9)$].¹⁹ However, whereas this holds for silicate network connectivities up to $\bar{N}_{BO}^{Si} \lesssim 2.9$, more polymerized glass networks that leave less interstitial space for PO_4^{3-} accommodation (e.g., those building the pore walls of MBGs;^{19,34,40,41} see the Supporting Information) are expected to promote phosphate ion clustering¹⁹ that eventually marks the onset of a macroscopic phase separation. Such an aggregation is likely already initiated in the P-richest structure of the $\bar{N}_{BO}^{Si} = 2.9$ series (as opposed to its other members) that reveals signs of glass-in-glass separation by SEM/EDS.²⁰ Moreover, preliminary ^{31}P NMR experiments evidenced a significantly faster 2QC buildup (data not shown), suggesting a pronounced phosphate clustering that is comparable with those of the MBGs. Yet, it remains unclear how much the nano/microscale separation in the $BG_{6.0}(2.9)$ glass structure stems from its particular preparation conditions and if (more) homogeneous glasses may result also for this composition with a modified melt-quench synthesis; we note that phosphate clustering is absent in the $BG_{4.0}(2.9)$ specimen, as witnessed by its equal b_{eff}^{exp} value as that of $BG_{4.0}(2.5)$.¹⁹

The few existing MD-based reports on the P atom distribution in BGs generally concluded closer-than-random P–P contacts,^{22–24} with the degree of phosphate clustering growing when either the P content of the BG or its silicate network connectivity is increased.^{22,23} Previous evaluations of

the phosphate-ion distribution compared the relative (average) numbers of Si and P atoms coordinated by the P sites, encoded in the factors $\mathcal{R}_{\text{Si-P}}^{\text{P-P}}(r) = \overline{\text{CN}}_{\text{P-P}} / \overline{\text{CN}}_{\text{Si-P}}^{\alpha}$,²⁴ where $\overline{\text{CN}}_{\alpha-\beta}$ represents the average coordination number of species α with respect to β over a radius r . $\mathcal{R}_{\text{Si-P}}^{\text{P-P}}(r) = 1$ implies that Si and P atoms distribute statistically (according to their respective number densities) around the P sites in the glass. Table S2 of the Supporting Information lists the $\mathcal{R}_{\text{Si-P}}^{\text{P-P}}$ ratios evaluated for the present BG_p($\bar{N}_{\text{BO}}^{\text{Si}}$) glass models with $r = 450$ pm and $r = 600$ pm; the latter radius was employed by Tilocca et al.^{22–24} The $\mathcal{R}_{\text{Si-P}}^{\text{P-P}}(600)$ data scatter around 1.4, in accordance with the value(s) reported for “45SS” [i.e., BG_{2.6}(2.1)] in ref 24 and suggesting closer P–P atom associations than those of statistically distributed phosphate species. However, in view of the data uncertainties, no significant trend is observed as either of p or $\bar{N}_{\text{BO}}^{\text{Si}}$ varies, altogether in full consistency with our other evaluations. The results of Table 2 together with Figures 5 and 6 offer some more concrete insight into the consequences of the observed $\mathcal{R}_{\text{Si-P}}^{\text{P-P}}(600)$ value for the spatial arrangements of the phosphate groups.

In summary, the P atom distribution in the modeled structures—and thereby also the physical samples, considering the excellent agreement between the NMR/MD derived effective dipolar coupling constants (Figure 3; Table 2)—are overall well-mimicked by a simple statistical distribution subject to a minimum P–P interatomic distance of $d_{\text{min}} \approx 360$ pm. Several parameters characterizing the P atom dispersion are captured well by the R(360) model, such as b_{eff} , \bar{r}_{min} , as well as $\{\bar{N}^{\text{C}}, \alpha_{\text{N}}^{\text{C}}\}$ when evaluated with $R^{\text{C}} \lesssim 460$ pm. Nevertheless, the results of Figures 5 and 6 underscore that the details of the P–P interatomic-distance array in the MD structures cannot strictly originate from a simple statistical distribution: the primary distinctions are reflected over the P–P distance-range of 450–600 pm, with the MD-derived phosphate-ion dispersion emphasizing closer interatomic contacts, whereas its distribution width σ_{min} over $\{r_{\text{min}}\}$ is generally narrower than the R(360) model (see Table 2). The discrepancies between the MD and random models reduces gradually as the P content of the BG is increased.

6. CONCLUDING REMARKS

The spatial phosphate ion distribution was explored in several Na–Ca–Si–P–O glass structures with variable silicate network connectivities and P contents. The present comparison of effective ^{31}P – ^{31}P dipolar couplings (b_{eff}) obtained from NMR experiments and MD simulations represents one of very few assessments^{57,63–65} of the accuracy of classical MD approaches for predicting medium-range (~ 1 nm) structural features in glasses against direct and element-specific experimental constraints. However, as the effective coupling is an *aggregate* parameter for the underlying P atom arrangement, several distinct distributions may yield comparable b_{eff} values. On the basis of the excellent agreement between the experimental/computational results, we exploited the structural models for reaching a more detailed picture of the phosphate ion dispersion.

When requiring (closest) P–P interatomic contacts of $R^{\text{C}} \leq 460$ pm between nearest neighbors, i.e., the range relevant to spot formation of clusters typically encountered in ordered orthophosphate phases, the P atom distribution observed by MD simulations is well-mimicked by a statistical intermixing

that prevails throughout all glasses incorporating ≤ 6 mol % P_2O_5 and silicate network connectivities $\bar{N}_{\text{BO}}^{\text{Si}} \leq 2.9$; this leads to structures dominated by isolated phosphate groups or pairs thereof, whereas triplets and larger phosphate aggregates only occur to non-negligible extents in glasses associated with relatively high P_2O_5 contents (≥ 4 mol %). The main discrepancies between the MD-generated and statistical P atom distributions become apparent across the 450–600 pm range, where the MD-derived models manifest closer P–P interatomic contacts. Consequently, if the cluster analysis allows P–P interatomic distances up to 480 pm among nearest neighbors within each phosphate aggregate, the MD glass models reveals larger average cluster sizes than those commensurate with a simple statistical PO_4^{3-} distribution, although this trend only becomes pronounced for BGs exhibiting high P content. Moreover, while the average size of the phosphate aggregates grows concurrently with the amount of P in the structure, the clustering *tendency* is somewhat higher at the lowest P_2O_5 content of ≤ 2 mol %, with the discrepancies between the MD and random models gradually reducing as the P content of the BG is increased.

In conclusion, the orthophosphate groups are closely associated with the silicate network, around which they distribute nearly statistically across the glass structure. Noteworthy, this scenario prevails for *both* bioactive ($\bar{N}_{\text{BO}}^{\text{Si}} \lesssim 2.6$) and nonbioactive compositions for the span of $\bar{N}_{\text{BO}}^{\text{Si}} \leq 2.9$ examined herein (for larger silicate network connectivities, extensive phosphate aggregation likely occurs, as discussed in ref 19 and section 5.2). Hence, our observed invariance of the P atom distribution on the silicate network connectivity (and thereby indirectly also the *in vitro* bioactivity) implies that the observed bioactivity reduction/loss when $\bar{N}_{\text{BO}}^{\text{Si}}$ increases beyond ≈ 2.6 (refs 26 and 32) must stem from the *globally* inhibited glass *degradation* associated with the highly polymerized silicate networks—that naturally also impedes the leaching of non-mobile species (such as Ca^{2+} and PO_4^{3-}) surrounding the various network fragments—as opposed to a reduced phosphate release originating directly from any pronounced phosphate ion clustering across a ~ 10 nm scale and beyond.

■ ASSOCIATED CONTENT

Supporting Information

Further information about the ^{31}P NMR experimentation, MD simulation parameters, as well as additional structural data is provided. This material is available free of charge via the Internet at <http://pubs.acs.org>.

■ AUTHOR INFORMATION

Corresponding Author

*E-mail: mattias.eden@mmk.su.se.

Notes

The authors declare no competing financial interest.

■ ACKNOWLEDGMENTS

This work was supported by the Swedish Research Council (contract 2010-4943) and the Faculty of Sciences at Stockholm University. We gratefully acknowledge NMR equipment Grants from the Swedish Research Council, and the Knut and Alice Wallenberg Foundation.

REFERENCES

- (1) Hench, L. L. Bioceramics: From Concept to Clinic. *J. Am. Ceram. Soc.* **1991**, *74*, 1487–1510.
- (2) Jones, J. R. Review of Bioactive Glass: From Hench to Hybrids. *Acta Biomater.* **2013**, *9*, 4457–4486.
- (3) Rahaman, M. N.; Day, D. E.; Bal, B. S.; Fu, Q.; Jung, S. B.; Bonewald, L. F.; Tomsia, A. P. Bioactive Glass in Tissue Engineering. *Acta Biomater.* **2011**, *7*, 2355–2373.
- (4) Hench, L. L.; Splinter, R. J.; Allen, W. C.; Greenlee, T. K. Bonding Mechanisms at the Interface of Ceramic Prosthetic Materials. *J. Biomed. Mater. Res.* **1971**, *2*, 117–141.
- (5) Edén, M. NMR Studies of Oxide-Based Glasses. *Annu. Rep. Prog. Chem., Sect. C: Phys. Chem.* **2012**, *108*, 177–221.
- (6) Yang, W.-H.; Kirkpatrick, R. J.; Turner, G. ^{31}P and ^{29}Si Magic Angle Sample-Spinning NMR Investigation of the Structural Environment of Phosphorus in Alkaline-Earth Silicate Glasses. *J. Am. Ceram. Soc.* **1986**, *69*, C222–C223.
- (7) Dupree, R.; Holland, D.; Mortuza, M. G.; Collins, J. A.; Lockyer, M. W. G. A MAS NMR Study of Network-Cation Coordination in Phosphosilicate Glasses. *J. Non-Cryst. Solids* **1988**, *106*, 403–407.
- (8) Lockyer, M. W. G.; Holland, D.; Dupree, R. NMR Investigation of the Structure of Some Bioactive and Related Glasses. *J. Non-Cryst. Solids* **1995**, *188*, 207–219.
- (9) Grussaute, H.; Montagne, L.; Palavit, G.; Bernard, J. L. Phosphate Speciation in $\text{Na}_2\text{O}-\text{CaO}-\text{P}_2\text{O}_5-\text{SiO}_2$ and $\text{Na}_2\text{O}-\text{TiO}_2-\text{P}_2\text{O}_5-\text{SiO}_2$ Glasses. *J. Non-Cryst. Solids* **2000**, *263*, 312–317.
- (10) Elgayar, I.; Aliev, A. E.; Boccacini, A. R.; Hill, R. G. Structural Analysis of Bioactive Glasses. *J. Non-Cryst. Solids* **2005**, *351*, 173–183.
- (11) Aguiar, H.; Solla, E. L.; Serra, J.; González, P.; León, B.; Almeida, N.; Cachino, S.; Davim, E. J. C.; Correia, R.; Oliveira, J. M.; et al. Orthophosphate Nanostructures in Bioactive $\text{SiO}_2-\text{P}_2\text{O}_5-\text{CaO}-\text{Na}_2\text{O}-\text{MgO}$ Glasses. *J. Non-Cryst. Solids* **2008**, *354*, 4075–4080.
- (12) Pedone, A.; Charpentier, T.; Malavasi, G.; Menziani, M. M. New Insights into the Atomic Structure of 45S5 Bioglass by Means of Solid-State NMR Spectroscopy and Accurate First-Principles Simulations. *Chem. Mater.* **2010**, *22*, 5644–5652.
- (13) Mercier, C.; Follet-Houttemane, C.; Pardini, A.; Revel, B. Influence of P_2O_5 Content on the Structure of $\text{SiO}_2-\text{Na}_2\text{O}-\text{CaO}-\text{P}_2\text{O}_5$ Bioglasses by ^{29}Si and ^{31}P MAS-NMR. *J. Non-Cryst. Solids* **2011**, *357*, 3901–3909.
- (14) Fujikura, K.; Karpukhina, N.; Kasuga, T.; Brauer, D. S.; Hill, R. G.; Law, R. V. Influence of Strontium Substitution on Structure and Crystallization of Bioglass® 45S5. *J. Mater. Chem.* **2012**, *22*, 7395–7402.
- (15) FitzGerald, V.; Pickup, D. M.; Greenspan, D.; Sarkar, G.; Fitzgerald, J. J.; Wetherall, K. M.; Moss, R. M.; Jones, J. R.; Newport, R. J. A Neutron and X-ray Diffraction Study of Bioglass® with Reverse Monte-Carlo Modelling. *Adv. Funct. Mater.* **2007**, *17*, 3746–3753.
- (16) Martin, R. A.; Twyman, H. L.; Rees, G. J.; Smith, J. M.; Barney, E. R.; Smith, M. E.; Hanna, J. V.; Newport, R. J. A Structural Investigation of the Alkali Metal Site Distribution within Bioactive Glass Using Neutron Diffraction and Multinuclear Solid State NMR. *Phys. Chem. Chem. Phys.* **2012**, *14*, 12105–12113.
- (17) Martin, R. A.; Twyman, H. L.; Rees, G. J.; Barney, E. R.; Moss, R. M.; Smith, J. M.; Hill, R. G.; Chibin, G.; Charpentier, T.; Smith, M. E.; et al. An Examination of the Calcium and Strontium Site Distribution in Bioactive Glasses Through Isomorphic Neutron Diffraction, X-ray Diffraction, EXAFS and Multinuclear Solid State NMR. *J. Mater. Chem.* **2012**, *41*, 2212–2223.
- (18) Fayon, F.; Duée, C.; Poumeyrol, T.; Allix, M.; Massiot, D. Evidence of Nanometric-Sized Phosphate Clusters in Bioactive Glasses as Revealed by Solid-State ^{31}P NMR. *J. Phys. Chem. C* **2013**, *117*, 2283–2288.
- (19) Mathew, R.; Turdean-Ionescu, C.; Svensson, B.; Izquierdo-Barba, I.; García, A.; Arcos, D.; Vallet-Regí, M.; Edén, M. Direct Probing of the Phosphate-Ion Distribution in Bioactive Silicate Glasses by Solid-State NMR: Evidence for Transitions between Random/Clustered Scenarios. *Chem. Mater.* **2013**, *25*, 1877–1885.
- (20) Mathew, R.; Svensson, B.; Tilocca, A.; Edén, M. Toward a Rational Design of Bioactive Glasses with Optimal Structural Features: Composition-Structure Correlations Unveiled by Solid-State NMR and MD Simulations. *J. Phys. Chem. B* **2014**, *118*, 833–844.
- (21) Pedone, A.; Malavasi, G.; Menziani, M. Computational Insight into the Effect of CaO/MgO Substitution on the Structural Properties of Phospho-Silicate Bioactive Glasses. *J. Phys. Chem. C* **2009**, *113*, 15723–15730.
- (22) Tilocca, A.; Cormack, A. N.; de Leeuw, N. H. The Structure of Bioactive Silicate Glasses: New Insights from Molecular Dynamics Simulations. *Chem. Mater.* **2007**, *19*, 95–103.
- (23) Tilocca, A.; Cormack, A. N. Structural Effects of Phosphorus Inclusion in Bioactive Silicate Glasses. *J. Phys. Chem. B* **2007**, *111*, 14256–14264.
- (24) Tilocca, A. Cooling Rate and Size Effects on the Medium-Range Structure of Multicomponent Oxide Glasses Simulated by Molecular Dynamics. *J. Chem. Phys.* **2013**, *139*, 114501.
- (25) Xiang, Y.; Du, J. Effect of Strontium Substitution on the Structure of 45S5 Bioglasses. *Chem. Mater.* **2011**, *23*, 2703–2717.
- (26) Edén, M. The Split Network Analysis for Exploring Composition-Structure Correlations in Multi-Component Glasses: I. Rationalizing Bioactivity-Composition Trends of Bioglasses. *J. Non-Cryst. Solids* **2011**, *357*, 1595–1602.
- (27) Strnad, Z. Role of the Glass-Phase in Bioactive Glass-Ceramics. *Biomaterials* **1992**, *13*, 317–321.
- (28) Hill, R. An Alternative View of the Degradation of Bioglass. *J. Mater. Sci. Lett.* **1996**, *15*, 1122–1125.
- (29) Mysen, B. O.; Ryerson, F. J.; Virgo, D. The Structural Role of Phosphorus in Silicate Melts. *Am. Mineral.* **1981**, *66*, 106–117.
- (30) Ohtsuki, C.; Kokubo, T.; Yamamuro, T. Mechanism of Apatite Formation on $\text{CaO}-\text{SiO}_2-\text{P}_2\text{O}_5$ Glasses in a Simulated Body Fluid. *J. Non-Cryst. Solids* **1992**, *143*, 84–92.
- (31) Salinas, A. J.; Martin, A. I.; Vallet-Regí, M. Bioactivity of Three $\text{CaO}-\text{P}_2\text{O}_5-\text{SiO}_2$ Sol-Gel Glasses. *J. Biomed. Mater. Res., Part A* **2002**, *61*, 524–532.
- (32) Lebecq, I.; Désanglois, F.; Leriche, A.; Follet-Houttemane, C. Compositional Dependence on the in Vitro Bioactivity of Invert or Conventional Bioglasses in the Si-Ca-Na-P System. *J. Biomed. Mater. Res., Part A* **2007**, *83*, 156–168.
- (33) O'Donnell, M. D.; Watts, S. J.; Hill, R. G.; Law, R. V. The Effect of Phosphate Content on the Bioactivity of Soda-Lime Phosphosilicate Glasses. *J. Mater. Sci.: Mater. Med.* **2009**, *20*, 1611–1618.
- (34) Leonova, E.; Izquierdo-Barba, I.; Arcos, D.; Lopez-Noriega, A.; Hedin, N.; Vallet-Regí, M.; Edén, M. Multinuclear Solid-State NMR Studies of Ordered Mesoporous Bioactive Glasses. *J. Phys. Chem. C* **2008**, *112*, 5552–5562.
- (35) O'Donnell, M. D.; Watts, S. J.; Law, R. V.; Hill, R. G. Effect of P_2O_5 Content in Two Series of Soda Lime Phosphosilicate Glasses on Structure and Properties: Part I: NMR. *J. Non-Cryst. Solids* **2008**, *354*, 3554–3560.
- (36) Sitarz, M.; Bulat, K.; Szumera, M. Influence of Modifiers and Glass-Forming Ions on the Crystallization of Glasses of the $\text{NaCaPO}_4-\text{SiO}_2$ System. *J. Therm. Anal. Calorim.* **2012**, *109*, 577–584.
- (37) Kreidl, N. Phase Separation in Glasses. *J. Non-Cryst. Solids* **1991**, *129*, 1–11.
- (38) Yan, X. X.; Yu, C. Z.; Zhou, X. F.; Tang, J. W.; Zhao, D. Y. Highly Ordered Mesoporous Bioactive Glasses with Superior in Vitro Bone-Forming Bioactivities. *Angew. Chem., Int. Ed.* **2004**, *43*, 5980–5984.
- (39) Lopez-Noriega, A.; Arcos, D.; Izquierdo-Barba, I.; Sakamoto, Y.; Terasaki, O.; Vallet-Regí, M. Ordered Mesoporous Bioactive Glasses for Bone Tissue Regeneration. *Chem. Mater.* **2006**, *18*, 3137–3144.
- (40) Gunawidjaja, P. N.; Lo, A. Y. H.; Izquierdo-Barba, I.; García, A.; Arcos, D.; Svensson, B.; Grins, J.; Vallet-Regí, M.; Edén, M. Biomimetic Apatite Mineralization Mechanisms of Mesoporous Bioactive Glasses as Probed by Multinuclear ^{31}P , ^{29}Si , ^{23}Na and ^{13}C Solid State NMR. *J. Phys. Chem. C* **2010**, *114*, 19345–19356.
- (41) Gunawidjaja, P. N.; Mathew, R.; Lo, A. Y. H.; Izquierdo-Barba, I.; García, A.; Arcos, D.; Vallet-Regí, M.; Edén, M. Local Structures of

Mesoporous Bioactive Glasses and Their Surface Alterations in Vitro: Inferences from Solid State Nuclear Magnetic Resonance. *Philos. Trans. R. Soc., A* **2012**, 370, 1376–1399.

(42) Mathew, R.; Gunawidjaja, P. N.; Izquierdo-Barba, I.; Jansson, K.; García, A.; Arcos, D.; Vallet-Regí, M.; Edén, M. Solid-State ^{31}P and ^1H NMR Investigations of Amorphous and Crystalline Calcium Phosphates Grown Biomimetically from a Mesoporous Bioactive Glass. *J. Phys. Chem. C* **2011**, 115, 20572–20582.

(43) Vallet-Regí, M.; Salinas, A. J.; Ramirez-Castellanos, J.; Gonzalez-Calbet, J. M. Nanostructure of Bioactive Sol-Gel Glasses and Organic-Inorganic Hybrids. *Chem. Mater.* **2005**, 17, 1874–1879.

(44) Johnson, J. A.; Benmore, C. J.; Holland, D.; Du, J.; Beuneu, B.; Mekki, A. Influence of Rare-Earth Ions on $\text{SiO}_2\text{--Na}_2\text{O--RE}_2\text{O}_3$ Glass Structure. *J. Phys.: Condens. Matter* **2011**, 23, 065404.

(45) Marin-Montesinos, I.; Brouwer, D. H.; Antonioli, G.; Lai, W. C.; Brinkmann, A.; Levitt, M. H. Heteronuclear Decoupling Interference During Symmetry-Based Homonuclear Recoupling in Solid-State NMR. *J. Magn. Reson.* **2005**, 177, 307–317.

(46) Saalwächter, K.; Ziegler, P.; Spyckerelle, O.; Haider, B.; Sommer, J.-U. ^1H Multiple-Quantum Nuclear Magnetic Resonance Investigations of Molecular Order Distributions in Poly-(Dimethylsiloxane) Networks: Evidence for a Linear Mixing Law in Bimodal Systems. *J. Chem. Phys.* **2003**, 119, 3468–3482.

(47) Saalwächter, K.; Lange, F.; Matyjaszewski, K.; Huang, C.-F.; Graf, R. BaBa-xy16: Robust and Broadband Homonuclear DQ Recoupling for Applications in Rigid and Soft Solids up to the Highest MAS Frequencies. *J. Magn. Reson.* **2011**, 212, 204–215.

(48) Saalwächter, K. Robust NMR Approaches for the Determination of Homonuclear Dipole-Dipole Coupling Constants in Studies of Solid Materials and Biomolecules. *ChemPhysChem* **2013**, 14, 3000–3014.

(49) Smith, W.; Forester, T. R. DL_POLY_2.0: A General-Purpose Parallel Molecular Dynamics Simulation Package. *J. Mol. Graphics* **1996**, 14, 136–141.

(50) Todorov, I. T.; Smith, W.; Trachenko, K.; Dove, M. T. DL_POLY_3: New Dimensions in Molecular Dynamics Simulations via Massive Parallelism. *J. Mater. Chem.* **2006**, 16, 1911–1918.

(51) Yashima, M.; Sakai, A.; Kamiyama, T.; Hoshikawa, A. Crystal Structure Analysis of β -Tricalcium Phosphate $\text{Ca}_3(\text{PO}_4)_2$ by Neutron Powder Diffraction. *J. Solid State Chem.* **2003**, 175, 272–277.

(52) Mathew, M.; Schroeder, L. W.; Dickens, B.; Brown, W. E. The Crystal Structure of $\alpha\text{-Ca}_3(\text{PO}_4)_2$. *Acta Crystallogr.* **1977**, B33, 1325–1333.

(53) Sudarsanan, K.; Young, R. A. Significant Precision in Crystal Structural Details. Holly Springs Hydroxyapatite. *Acta Crystallogr.* **1969**, B25, 1534–1543.

(54) Ben Amara, M.; Vlasse, M.; Le Flem, G.; Hagenmuller, P. Structure of the Low-Temperature Variety of Calcium Sodium Orthophosphate, NaCaPO_4 . *Acta Crystallogr.* **1983**, C39, 1483–1485.

(55) Zwanziger, J. W.; McLaughlin, J. C.; Tagg, S. L. Sodium Distribution in Sodium Tellurite Glasses Probed with Spin-Echo NMR. *Phys. Rev. B* **1997**, 56, 5243–5249.

(56) Alam, T. M.; McLaughlin, J.; Click, C. C.; Conzone, S.; Brow, R. K.; Boyle, T. J.; Zwanziger, J. W. Investigation of Sodium Distribution in Phosphate Glasses Using Spin-Echo ^{23}Na NMR. *J. Phys. Chem. B* **2000**, 104, 1464–1472.

(57) Du, J.; Cormack, A. N. The Medium Range Structure of Sodium Silicate Glasses: A Molecular Dynamics Simulation. *J. Non-Cryst. Solids* **2004**, 349, 66–79.

(58) Schmedt auf der Günne, J.; Eckert, H. High-Resolution Double-Quantum ^{31}P NMR: A New Approach to Structural Studies of Thiophosphates. *Chem.—Eur. J.* **1998**, 4, 1762–1767.

(59) Lin, K. S. K.; Tseng, Y.-H.; Mou, Y.; Hsu, Y.-C.; Yang, C.-M.; Chan, J. C. C. Mechanistic Study of Apatite Formation on Bioactive Glass Surface Using ^{31}P Solid-State NMR Spectroscopy. *Chem. Mater.* **2005**, 17, 4493–4501.

(60) Ren, J.; Eckert, H. DQ-DRENAR: A New NMR Technique to Measure Site-Resolved Magnetic Dipole-Dipole Interactions in

Multispin-1/2 Systems: Theory and Validation on Crystalline Phosphates. *J. Chem. Phys.* **2013**, 138, 164201.

(61) Schmedt auf der Günne, J. Effective Dipolar Couplings Determined by Dipolar Dephasing of Double-Quantum Coherences. *J. Magn. Reson.* **2006**, 180, 186–196.

(62) Eckert, H.; Elbers, S.; Epping, J. D.; Janssen, M.; Kalwei, M.; Strojek, W.; Voigt, U. Dipolar Solid State NMR Approaches Towards Medium-Range Structure in Oxide Glasses. *Top. Curr. Chem.* **2005**, 246, 195–233.

(63) Olivier, L.; Yuan, X.; Cormack, A. N.; Jäger, C. Combined ^{29}Si Double Quantum NMR and MD Simulation Studies of Network Connectivities of Binary $\text{Na}_2\text{O--SiO}_2$ Glasses: New Prospects and Problems. *J. Non-Cryst. Solids* **2001**, 293–295, 53–66.

(64) Voigt, U.; Lammert, H.; Eckert, H.; Heuer, A. Cation Clustering in Lithium Silicate Glasses: Quantitative Description by Solid-State NMR and Molecular Dynamics Simulations. *Phys. Rev. B* **2005**, 72, 064207.

(65) Jaworski, A.; Stevansson, B.; Pahari, B.; Okhotnikov, K.; Edén, M. Local Structures and Al/Si Ordering in Lanthanum Aluminosilicate Glasses Explored by Advanced ^{27}Al NMR Experiments and Molecular Dynamics Simulations. *Phys. Chem. Chem. Phys.* **2012**, 14, 15866–15878.